Indian Journal of Pure & Applied Physics
Vol. 64, July 2026, pp. 803-816
DOI: 10.56042/ijpap.v64i7.30495

Fractional-Order PID Based Outer Loop Control for G2V/V2G Systems in Plug-in Electric Vehicle Applications

Abhishek Kumar*, Surya Prakash & Madhu Singh

Department of Electrical Engineering, National Institute of Technology, Jamshedpur 831 014, India

Received: 15th April 2026; accepted: 3rd June 2026

The increasing adoption of Plug-in Electric Vehicles (PEVs) and the rise of Grid-to-Vehicle (G2V) and Vehicle-to-Grid (V2G) technologies require highly robust and efficient bidirectional AC–DC converters capable of maintaining stable DC-link voltage and high-power quality. Conventional proportional–integral (PI) controllers remain widely used for outer-loop regulation; however, their integer-order nature limits performance under abnormal grid and input conditions, and abrupt bidirectional power-flow transitions. To address these limitations, this work proposes a fractional-order proportional–integral–derivative (FOPID) controller as the outer-loop regulator for a bidirectional AC–DC converter supporting G2V/V2G operation. To improve resilience to grid disruptions, parameter uncertainties, and system nonlinearities, fractional orders are analytically adjusted. The suggested FOPID controller greatly enhances transient response, steady-state accuracy, DC-link voltage stability, and total harmonic distortion (THD), according to a comparison with the traditional PI controller. The FOPID-based scheme's practical efficacy is confirmed by hardware-in-the-loop validation, which shows improved overall performance for real-time PEV charging and V2G support as well as smoother bidirectional transitions.

Keywords: Plug-in electric vehicle (PEV), Bidirectional power flow, FOPID controller, DC-link voltage control, Total harmonic distortion (THD)

1 Introduction

The electrification of the transportation industry has emerged as a major avenue through which to reduce greenhouse gas, air pollution and reliance on traditional fossil sources of energy[1]. The key element of this change has become PEVs, which can help mitigate the emission of greenhouse gas to a considerable extent, enhance energy efficiency, and reduce dependency on fossil fuels[1-2]. In comparative terms with the ordinary internal combustion engine vehicle, PEVs offer many benefits, such as high efficiency, less operating noise, and the ability to be powered by various sources of renewable energy, which makes it a popular choice and a major one to adopt on a massive scale[2]. Electric vehicles can broadly be categorized into two types: (i) hybrid electric vehicles (HEVs) that incorporate an internal combustion engine with an electric propulsion system, and (ii) battery electric vehicles (BEVs) that operate only using stored electric power[3]. HEVs use regenerative braking, which allows them to recover kinetic energy when accelerating. BEVs only charge their batteries using an external charging system, making them fully dependent on available external power electronics interfaces to charge their batteries[4-5]. A DC-DC converter is essential to provide efficient charging and stability to the operation of the EVs, as they control the level of voltage and offers the battery management system with very high stability of the power flow. Buck-boost, Cuk, and SEPIC converters have been popular traditional converter topologies because of their robustness, design flexibility and ability to assist voltage regulation across various operating conditions[5-6]. At the same time, the world power systems are slowly switching to a solution of bidirectional power flow, especially by the use of G2V and V2G topologies. These interfaces allow electric vehicles to both extract electrical energy from the grid and return stored energy at peak demand, thereby facilitating peak shaving, frequency regulation, and enhanced load management[7-9]. Such coordinated bidirectional operation transforms EVs into distributed energy storage units, enhancing grid resilience, reliability, and flexibility. The majority of the bidirectional chargers utilize a cascaded control architecture, which consists of an inner current-control loop and an outer voltage or power-control loop[10]. While the inner loop ensures fast dynamic current regulation, the outer loop plays a decisive role in maintaining DC-link voltage stability, minimizing

*Corresponding author: E-mail: abhishekumar218@gmail.com

grid current total harmonic distortion, and ensuring smooth transitions between G2V and V2G modes[11]. Conventional proportional–integral (PI) controllers remain the dominant choice for outer-loop regulation due to their simplicity[12].

However, their fixed integer-order structure limits their robustness and tuning flexibility under nonlinear battery dynamics, uncertain grid conditions, and abrupt bidirectional power-flow transitions. Although several advanced nonlinear and intelligent control methods have been proposed, including sliding-mode control, model predictive control, and AI-based approaches, many of these suffer from practical drawbacks such as chattering, high computational complexity, model dependence, and challenges in ensuring stability margins[13-15]. Recent progress in digital implementation has also made implementation of fractional-order controllers more uncomplicated in real-time embedded applications, and therefore they are a suitable option in PEV charging and grid-interfaced power electronic systems.

To overcome these limitations, FOPID controllers have emerged as an effective alternative by introducing fractional-order integral (μ) and derivative (β) terms, which provide additional tuning flexibility and enable more precise control of system dynamics under uncertain operating conditions[16]. Owing to their superior dynamic response, robustness, and adaptability, FOPID controllers have attracted significant attention in power-system and renewable-energy applications. For instance, comparative studies between conventional PID and FOPID controllers in single-area and two-area load frequency control systems have demonstrated the improved performance of FOPID-based schemes[24-25]. Similarly, FOPID has been applied as an inner-loop controller in load frequency control for grid-connected PV–wind hybrid systems. In another study, a State Machine-based Fractional Order PID (FO-PID) controller optimized using Particle Swarm Optimization (PSO) was proposed for multilevel inverter applications[26]. Furthermore, Mother Optimization Algorithm-based FOPID control has been implemented in zeta converter-based DC–DC converters for electric vehicle applications[27]. These studies collectively demonstrate the capability of FOPID controllers to improve system stability, robustness, and transient performance in complex nonlinear systems.

Motivated by these advantages, this paper proposes a FOPID-based outer-loop control strategy for the grid-side inverter in bidirectional electric vehicle (EV) charging and discharging operations. Unlike conventional PI/PID controllers commonly employed in Grid-to-Vehicle (G2V) and Vehicle-to-Grid (V2G) control strategies, the proposed controller incorporates fractional-order integral (μ) and derivative (β) parameters, thereby providing two additional degrees of freedom for controller tuning. This enhanced flexibility enables more accurate shaping of system dynamics, improved adaptability under varying operating conditions, and superior performance during bidirectional power-flow transitions.

Despite the several control strategies that have been developed for bidirectional AC–DC converters in PEV charging applications, notable limitations persist in the existing literature. Conventional PI controllers are still the most used, being simple in nature and easy to apply, but they perform poorly in the presence of nonlinear battery dynamics, uncertain grid impedance, and sudden reversals in power-flow characteristic of G2V/V2G operation. Advanced nonlinear techniques that have been investigated to enhance transient response are the sliding-mode control, model predictive control and intelligent techniques. Nevertheless, these techniques usually have disadvantages such as chattering, high computational cost, and complicated tuning processes, as well as depending on accurate modelling of the system.

Fractional-order controllers have proven to exhibit enhanced robustness and dynamic performance in a range of power-electronic systems, but have been little used as outer-loop controllers in grid-connected bidirectional chargers of PEVs. Specifically, few studies have been done on DC-link voltage stability, quality of grid current, reduction of THD, and resilience in bidirectional operation transition.

2 Materials and Methods

2.1 System Configuration

The system configuration of a single-phase voltage source converter (VSC) and a bidirectional DC-DC converter (BDDC) for a grid-to-vehicle application is shown in Fig. 1. This system provides a seamless transition of energy transfer from grid-to-vehicle or

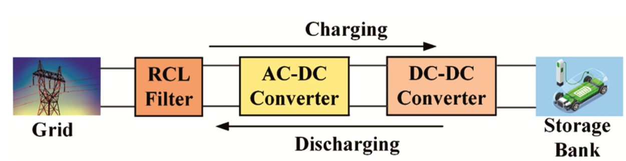

Fig. 1 — Block diagram of G2V/V2G system

vice-versa. Depending on the state of the grid, an STS switch is used to connect or disconnect the grid from the utility grid. A nonlinear load is realized by connecting an R-L load across a single-phase bridge rectifier. A series inductor is connected between the VSC and the grid at the PCC, which suppresses grid harmonics. Moreover, the R-C ripple filter suppresses voltage harmonics generated due to VSC switching. These VSC and BDDC are connected on a common DC-link (Vdc). The BDDC system operates as a charging in buck mode for discharging and in boost mode.

2.2 Bidirectional DC-DC Converter (BDDC)

The BDDC system comprises the following interconnected components: The voltage regulation module employs a BDDC converter to maintain a stable intermediate bus voltage. The battery management system ensures the safe and effective functioning of the electric vehicle battery. The controller switch chooses the charging and discharging operational mode and activates the suitable circuit paths. Voltage second balance equation for an inductor.

$$v_{in}\,D + (v_o) - (1 - D) = 0 \quad \text{... (1)}$$

$$v_0 = \frac{D}{(1-D)} \times v_{in} \quad \text{... (2)}$$

In Eq. (1), v_b denotes the input voltage, v_{dc} denotes the output voltage, and D denotes the duty cycle. The proportion of time that the switch remains ON within each cycle is altered to regulate the switch as well as to obtain a desired output voltage, which is called the duty cycle. The duty cycle and the application requirements provide the input and output voltages. In order to ensure accurate steady voltage regulation, such an adjustment is often controlled by a pulse-width modulation controller that varies the switching ON and OFF time depending on feedback of the output. Furthermore, the state of charge (SoC_b) of the battery is required for the system operating, which controls the operation of the plug-in electric vehicle as well as the battery[17]. This operation can be classified into the following cases.

i When $SoC_{min} < SoC_b < SoC_{max}$

The control strategy is split into two conditions;

- If the generated power P_g, when the load demand is less than the load capacity P_L, the excessive power is utilized in charge the battery, and the converter operates to retrieve the optimal power.
- If P_g is less than P_L, the battery is added to assist the load and the converter is kept on its optimal power.

ii When the above condition is not satisfied

The control will be further be categorized as follows;

- If $SoC_b \leq SoC_{min}$, to avoid excessive battery discharging, load shedding is implemented.
- If $SoC_b \geq SoC_{max}$, to use only the necessary amount of power, the converter has a reference to the all-charged battery, which indicates that its operation is based on grid-to-vehicle and vehicle-to-grid modes to supply only the necessary amount of power.

2.3 VSC System for G2V and V2G Plug-in Electric Vehicle

The primary problem in the contact between the grid and AC-DC converter in the energy transfer modes between and among G2V and V2G as shown in Fig. 2. The positive current flow in the grid to an AC-DC converter. The grid voltage is defined as a time-related sinusoidal voltage waveform in phase configuration:

$$V = V_p \sin(\omega t + \theta) \quad \text{... (3)}$$

If θ is positive value of reactive power indicates that the converter supplies reactive power to the grid, whereas a negative value implies that reactive power is drawn from the grid to meet the converter's reactive demand. Fig. 3 (c) - (f). Inductive and capacitive charging operating modes.

$$v_c(t) = \sqrt{2}V_c \sin(\omega t - \delta) \quad \text{... (4)}$$

where V_c is the rms value of the fundamental component of the converter voltage $v_c(t)$, and δ represents the phase displacement between $v_c(t)$ and $v_s(t)$. The resulting grid current is expressed as,

$$I_g(t) = \sqrt{2}I_s \sin(\omega t - \theta) \quad \text{... (5)}$$

where θ is the angle between $I_g(t)$ and $v_c(t)$

As Figs. 3 (a) and (b) shows, the grid will provide an active power, whenever $v_c(t)$ lags $v_s(t)$, and it is

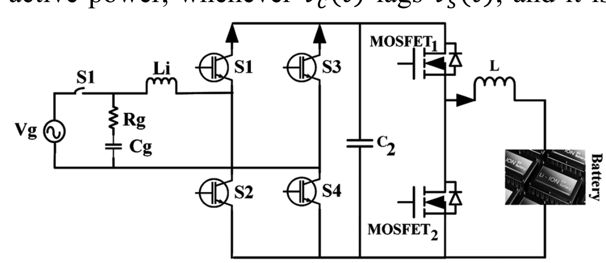

Fig. 2 — Circuit diagram of a single phase of G2V/V2G topology

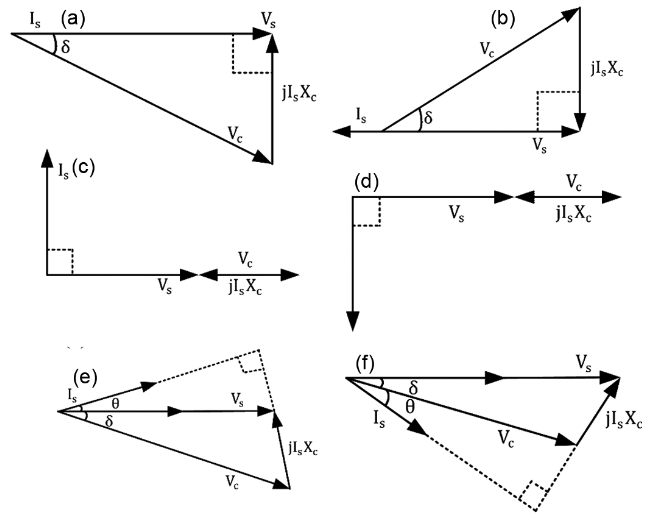

Fig. 3 — Vector diagram representing various operating modes of G2V/V2G system

delivered to the grid whenever $v_s(t)$ lags $v_c(t)$. Since $v_c(t)$ and $v_s(t)$ are sinusoidal, $i_g(t)$ is also sinusoidal. These are defined by their phase angle θ, which determines the direction of the reactive power flow[18].

2.4 Power Converters

To enhance the voltage output of the grid-connected bidirectional DC-DC converter (BDDC) is employed between the converter and the grid. This BDDC converter is also tasked with both the side power supply of the system. The decline in power conversion efficiency due to cascaded power stages is somewhat offset by enhanced extraction efficiency[19]. The choice of switching device mostly relies on the blocking voltage, ON-state resistance, and switching frequency. Below 600 V, MOSFETs have reduced conduction losses in comparison to insulated-gate bipolar transistor (IGBTs). IGBTs are favoured for voltages exceeding 600 V due to their reduced conduction losses. The implementation of wide-bandgap devices (GaN and SiC) enables an increase in switching frequency. These devices have reduced parasitic effects, resulting in enhanced switching performance[20]. The thermal properties of these devices are superior, facilitating the installation of high-density power converters. The main objective of this field study is to examine different topologies and device performance at various power levels.

2.5 Decoupling Capacitor

Regardless of the topology utilized to implement the converter. The DC-link voltage undergoes a second harmonic ripple to maintain instantaneous power balance. The decoupling capacitor size is determined by this ripple. The following formula can be used to determine the decoupling capacitor size.

$$C_{dc} = \frac{P_g}{2\times\omega_g\times V_{dc}\times\Delta v_{dc}} \quad \ldots (6)$$

where ω_g is the grid angular frequency, $V_{dc}$is the DC-link voltage, Δv_{dc} is the ripple of the DC-link voltage P_g is the output power of the grid[21]. The following details can be deduced from this equation, which provides the theoretical minimum capacitance value.

i With the increase in the grid power, for a constant DC-link voltage and Δv_{dc}, capacitance requirement also increases.

ii When the decoupling is higher than the DC-link voltage, a smaller capacitor can be used to achieve the same decoupling.

iii The dc-link capacitance is raised to have a very small ripple in the dc-link voltage Δv_{dc},

This decoupling capacitor size has an impact on the converter power density. There are several sophisticated power decoupling circuits and techniques described in the literature to decrease the capacitor size.

2.6 RCL- Filter

The grid-side converter of a grid-connected inverter inherently generates harmonics around the switching frequency[22]. These harmonics cannot be directly injected into the utility grid because the system must comply with the harmonic limits defined. Therefore, a low-pass filter (LPF) is installed at the inverter output to mitigate harmonic distortion before grid integration. The LPF should be designed to ensure several key characteristics: significant attenuation at the switching frequency (approximately −40 dB), unity gain at the fundamental frequency, demonstrate resilience to external parameter perturbation, achieve effective harmonic suppression while constraining electromagnetic interference, and sustain minimum voltage deviation and power dissipation within the filter stage[23].

2.7 Control techniques for BDDC System

In this technique, the battery is charged and discharged using a bidirectional DC-DC converter (BDDC), and PWM control is employed. A PI controller is implemented to regulate the output current of the battery. A proportional-integral controller calculates the desired charging current reference setpoint[24].

$$I_{cmd} = K_p\left(V_{ref} - V_{bat}\right) + K_i \int\left(V_{ref} - V_{bat}\right) dt \quad \dots (7)$$

Here, V_{ref} represent the reference voltage, V_{bat} denotes the measured battery voltage and K_p and K_i are the PI gains of the PI controller. This approach is suitable for both buck and boost modes. A fixed frequency (fs) saw-tooth carrier waveform is used in evaluating the controller output to obtain the switching signals for the switches in the BDDC converter.

$$I_{bat} = \begin{cases} I_{cmd,}\ during\ G2V \\ -I_{cmd,}\ during\ V2G \end{cases} \quad \dots (8)$$

For bidirectional operational modeling G2V and V2G electric vehicle design.

In the discharging operation, the battery supplies power to the grid.

$$P_{v2g} = V_{bat} \times I_{V2g} \quad \dots (9)$$

where, P_{v2g} represents the real power supplied from the electric vehicle to the grid.

In the charging operation, power supplies to the vehicle.

$$P_{g2v} = V_{grid} \times I_{cmd} \quad \dots (10)$$

where, I_{cmd} represents the battery charging current, V_{grid} represent grid voltage.

2.8 Conventional PI outer Loop Controller

The outer loop of the DC-link voltage regulation plays a crucial role in maintaining energy balance between the AC grid and the DC-link capacitor of the single-phase grid-connected converter (SGcC). Its primary objective is to ensure that the average active power drawn from the DC side equals the active power injected into the AC grid. From the power expressions in Eq. (11).

$$\left.\begin{aligned} P_{AC} &\approx \frac{V_g I_g^*}{2} \\ P_{DC} &= V_{dc} I_{dc} \end{aligned}\right\} \rightarrow I_{dc} \approx \frac{V_g}{2V_{dc}^*} I_g^* = G I_g^* \quad \dots (11)$$

The average DC-link current can be expressed as

$$i_{dc} = (1 - u) i_g \quad \dots (12)$$

where u is the converter switching function generated by the inner current control. Under unity power factor operation and neglecting converter losses and DC-voltage ripple, the AC and DC power satisfy $P_{AC} \approx P_{DC}$ allowing the power transfer gain to be approximated as a constant $G = \frac{V_g}{2V_{dc}^*}$. This simplified model implies that converter nonlinearities are small and that the inner current control loop is substantially faster than the outer DC-link voltage loop[25]. Under this linearized relationship, the DC-link voltage control block diagram is shown in Fig. 4. The resultant characteristic equation $(s^2 \left(\frac{GK_p}{C}\right) s + \left(\frac{GK_p}{C}\right)) = 0$.

The PI proportional and integral gains can be de deduced by identifying this characteristic equation in its canonical form $s^2 + 2\xi\omega_n s + \omega_n^2 = 0$. The proportional and integral gains of the PI outer loop can be determined. The transient response, overshoot and settling of DC-link voltage can be pre-shaped using the damping ratio and natural frequency applied. PI also has the disadvantage of having low tuning bandwidth, particularly in nonlinear or non-integer-order control (e.g. power converters) where integer-order dynamics are to be satisfied and tuning limits must be computed concerning the tuning-dependent effectiveness of robustness and disturbance rejection. Practically, PI controllers can cause improper parameter variation (e.g. capacitor ageing, variable grid conditions), reduced settling time and lack of dynamic flexibility. This is successfully done through the use of FOPID, where non-integer order of the derivative and the integral gives more degrees of

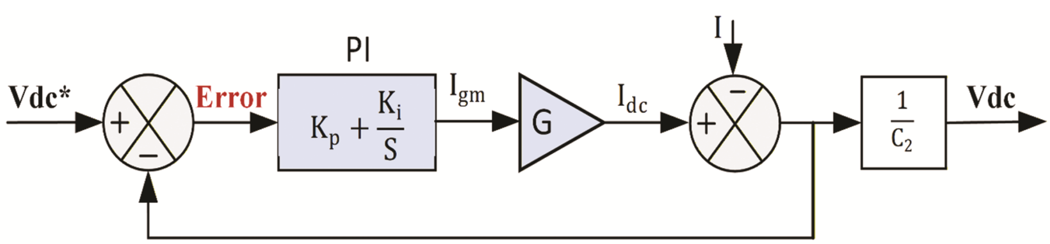

Fig. 4 — Conventional PI controller for outer-loop G2V/V2G system

freedom, resulting in control precision, high robustness and performance in a broader application across dynamic systems.

2.9 Proposed FOPID-Based Outer-Loop Controller, System Modeling, and Control Strategy

The fractional calculus introduces operators of non-integer order, enabling finer shaping of both the magnitude and phase of the control system [26-27]. The FOPI and FOPID controllers generalizes the conventional PI by replacing the integrator with a fractional integrator s^{μ} and optionally adding a derivative term S^{β}. The general form is

$$G_{FOPID}(S) = K_P + \frac{K_I}{S^{\mu}} + K_D S^{\beta} \quad \text{... (13)}$$

To regulate the bidirectional power flow and improve dynamic performance, a FOPID controller is employed. The FOPID controller is an advanced control technique used to improve the dynamic and steady-state performance of power electronic system. Compared with the conventional PID controller, the FOPID controller provides additional flexibility through fractional integral and derivative orders, resulting in better robustness, reduced overshoot, and improved stability.

In the proposed system, the DC-link voltage V_{dc} is regulated using a FOPID controller shown in Fig. 5. The error signal is generated by comparing the reference DC-link voltage with the measured DC-link voltage and expressed as;

$$e(t) = V_{dc}^{*} - V_{dc} \quad \text{... (14)}$$

where V_{dc}^{*} is the reference DC-link voltage and V_{dc} is actual DC-link voltage. The control output of the FOPID controller is given by;

$$u(t) = K_p e(t) + K_i D^{-\mu} e(t) + K_d D^{\beta} e(t) \quad \text{... (15)}$$

where K_p is proportional gain, K_i is integral gain, K_d is derivative gain. The plant shown in the control block diagram consists of a gain block G and capacitor dynamics represented by $1/G_{FOPID}(s)$. Therefore, the plant transfer function is expressed as;

$$P(s) = \frac{G}{G_{FOPID(S)}} \quad \text{... (16)}$$

The open-loop transfer function of the complete system is obtained by multiplying the controller transfer function and plant transfer function;

$$L(s) = G_{FOPID}(s)P(s) \quad \text{... (17)}$$

$$L(s) = \left(K_P + \frac{K_I}{S^{\mu}} + K_D S^{\beta}\right)\frac{G}{G_{FOPID(S)}} \quad \text{... (18)}$$

Substituting the open-loop transfer function,

$$T(s) = \frac{\left(K_P + \frac{K_I}{S^{\mu}} + K_D S^{\beta}\right)\frac{G}{G_{FOPID(S)}}}{1 + \left(K_P + \frac{K_I}{S^{\mu}} + K_D S^{\beta}\right)\frac{G}{G_{FOPID(S)}}} \quad \text{... (19)}$$

The controller parameters K_P, K_i and K_d are determined using tuning method such as Ziegler-Nichols tuning[28]. Initially, the integral and derivative gains are set to zero, and the proportional gain is gradually increased until sustained oscillations occur. Let K_u denote the ultimate gain and P_u denotes the oscillation period. The controller parameters are then calculated as;

$$K_P = 0.6K_u, K_i = \frac{2K_P}{P_u} \text{ and } K_d = \frac{K_P P_u}{8} \quad \text{... (20)}$$

The fractional integral order μ and β is the fractional derivative order are selected based on system performance requirements such as settling time, overshoot and robustness.

The fractional integral order primarily influences steady-state accuracy and robustness. First-order plant μ is commonly selected within the range in Fig. 6.

$$\left.\begin{aligned} P_{AC} &\approx \frac{V_g I_g^{*}}{2} \\ P_{DC} &= V_{dc} I_{dc} \end{aligned}\right\} \rightarrow I_{dc} \approx \frac{V_g}{2V_{dc}^{*}} I_g^{*} = G I_g^{*}$$

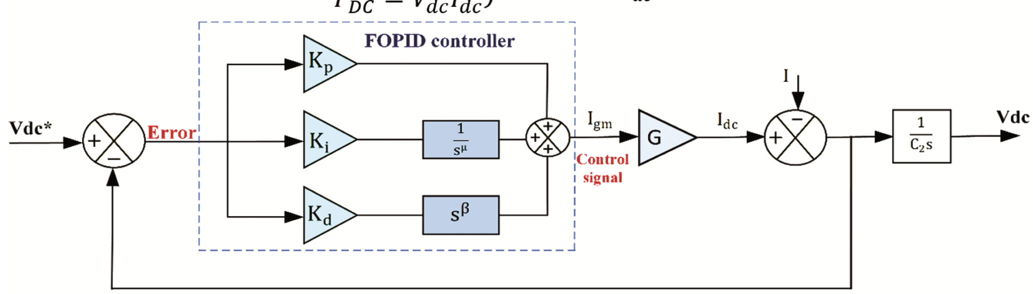

Fig. 5 — Proposed FOPID controller for outer-loop G2V/V2G system

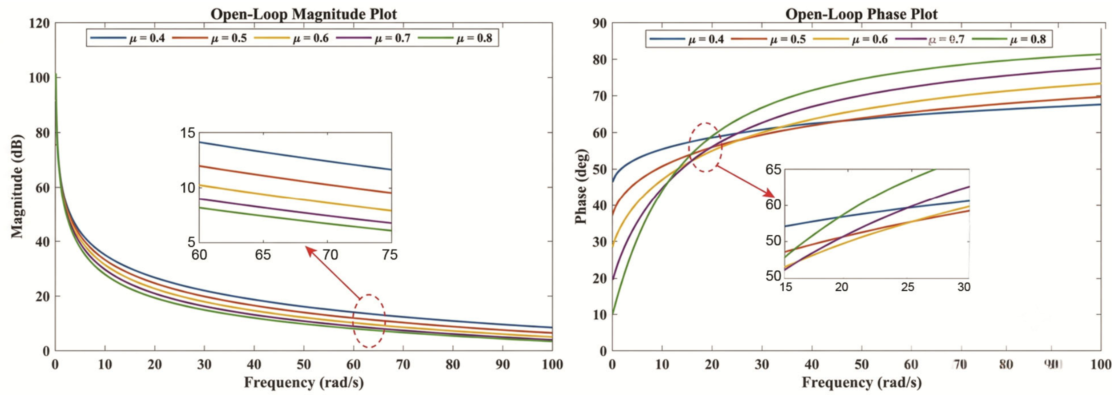

Fig. 6 — Frequency response of different values of □ for the proposed FOPID system

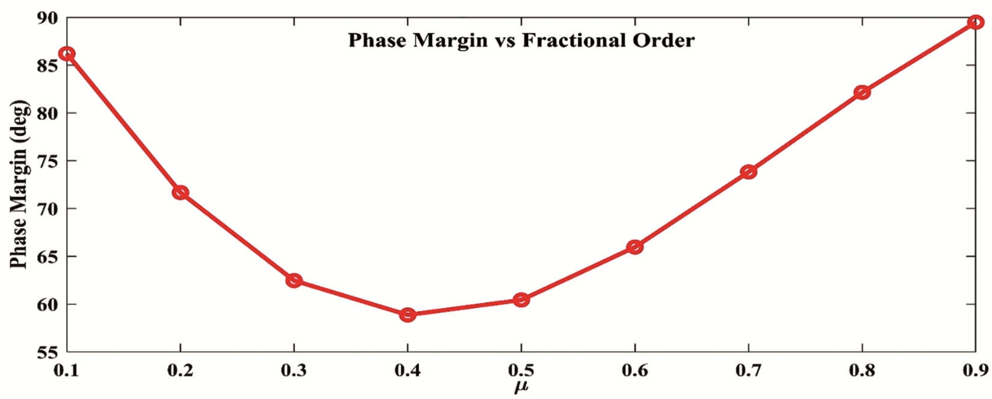

Fig. 7 — Phase margin vs fractional order for FOPID controller with different values of μ

$0.4 \leq \mu \leq 1$

where smaller values improve robustness at the expense of response speed. Derivative order affects transient performance and noise sensitivity. Typical design choices are;

$0.5 \leq \beta \leq 1$

The Fractional integrator contributes,

$\angle s^{-\mu} \approx -90^0 \mu$

which makes it possible to finely adjust phase and gain margins without the constraints of integer-order behavior. This leads to improved disturbance attenuation, better robustness, and more flexible control of dynamic performance. Moreover, the fractional derivative order contributes approximately

$\angle s^{\beta} \approx 90^0 \beta$

which enables flexible phase compensation beyond conventional integral-order PID controllers. This additional tuning freedom improves damping performance, transient stability, and dynamic response adaptability.

Frequency-response analysis demonstrates that increasing μ (toward 1) increases the phase margin and attenuates gain near the crossover frequency.

Based on the observed trends from the bode plots and the phase margin in Fig. 7. The phase margin decreases from $\mu = 1 \; to \; 0.4$. at $\mu = 0.5$. The system achieves stable and balanced performance. Beyond $\mu = 0.5$, stability margin continues to increase. Thus, a recommended design value is $\mu = 0.5$. which provides a balanced tradeoff between robustness, dynamic response, and stability. Similarly, the system achieves balanced dynamic performance for values around $\beta = 0.8$. which provides a suitable tradeoff between fast transient response, damping capability, and acceptable noise sensitivity.

The proposed system takes advantage of the DC-link voltage Vdc to produce a synchronized AC voltage v_g and deliver the power into the grid and local loads. It consists of six-switching devices, $S_1 \; to \; S_4$, operating at a switching frequency f_s. A filter of inductors absorbs the content at high frequency, and grid harmonic requirements are achieved. A phase-locked loop (PLL), inner loop and outer loop controller control the power injection and synchronization with the grid[29]. In this paper, the hysteresis current control methods are used as the inner loop. The objective is to make sure that the output current of the inverter i_g is closely synchronized with one reference current i_g^*, which tends to be generated according to the grid voltage and required power injection. The interface inductor i_g and optionally includes a small resistance r_g, which is winding or parasitic resistance, derive the inverter to the grid. The dynamic nature of the system can be modelled using the KVL law about the inverter output and the point of connection to the output voltage of the inverter v_i, the grid voltage v_g, and the filter inductor current i_i is related by

$$v_i = L_g = \frac{di_g}{dt} + r_f i_g + v_g \qquad \text{... (21)}$$

Rearranging the above equation yields the state-space representation of the current dynamics.

$$\frac{di_g}{dt} = \frac{1}{L_g}\left(v_i - v_g - r_f i_g\right) \qquad \text{... (22)}$$

To regulate the DC-link voltage at a set reference value, an FOPID control is utilised. The system uses a loss current component i_L. In addition, battery charging contributes to the total current demand, and its equivalent component can be estimated as;

$$i_{bat} = \frac{v_d^b i_d^b}{v_{gm}} \qquad \text{... (23)}$$

The reference current for grid injection i_g^* can be derived as;

$$i_g^* = i_{bat} + i_L \qquad \text{... (24)}$$

For the current regulation, a hysteresis-band current control strategy is adopted. In this method, the actual current i_g, oscillates within a tolerance band $\pm h_i$ around the reference current i_g^*. The switching logic for the inverter operates as follows;

i. If $i_g > i_g^* \pm h_i$, the upper switch in the inverter leg is turned off, and the inverter output voltage is forced toward the negative side $v_i = -\frac{v_{dc}}{2}$
ii. If $i_g < i_g^* \pm h_i$, the upper switch is turned on, pushing $v_i = \frac{v_{dc}}{2}$.

The switching behaviour is nonlinear and piecewise, but it ensures fast tracking with minimal steady-state error Fig. 8. illustrates the implementation of a phase-shift control scheme for the regulation of the DC-DC converter. The power transmitted through the DC-DC stage is contingent upon the phase disparity between the voltage waveforms of the primary and secondary bridges. A reference PEV voltage signal is established based on the system's needs to attain closed-loop control. The discrepancy between the reference PEV voltage signal and the measured PEV voltage output is calculated as the control error. The error is subsequently handled by the PI controller, which modifies the phase-shifting angle correspondingly. The controller regulates bidirectional power flow by adjusting the phase displacement between the bridges, hence ensuring steady output performance under fluctuating load or input conditions.

3 Results and Discussion

The effectiveness and performance of the proposed FOPID controller are evaluated through the G2V and V2G system. The system was modelled and evaluated in MATLAB/Simulink. The system running time is chosen at 2 sec. The detailed specifications of the proposed system parameters are listed in Table 1. Two test scenarios are executed to validate and assess the proposed system, including:

i Scenario 1: Taking power from the grid, Grid-to-Vehicle (G2V)

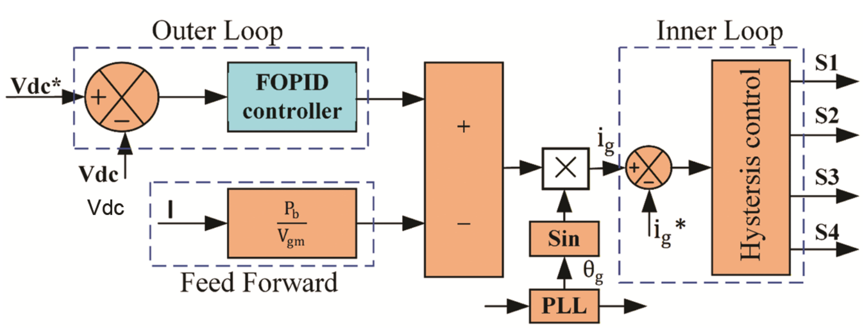

Fig. 8 — Control diagram of G2V/V2G system with proposed FOPID controllerRepresents a grid-based converter control shown in Fig. 8. A FOPID controller is used to adjust active power by processing the error in the dc-link voltage. The magnitude of the grid voltage, yielding a feed-forward, improves the dynamic response. Phase information on a phase-locked-loop (PLL) is used to produce the reference grid current. A hysteresis current controller is used to generate a switching signal to ensure accurate current tracking.

ii Scenario 2: Supplying power to the grid, Vehicle-to-Grid (V2G)

iii Scenario 3: Comparison of FOPID and PI controller

These scenarios are chosen to cover steady-state and transient conditions, ensuring thorough validation of the FOPID controller for the proposed system's effectiveness.

Table 1 — System parameters of the proposed system

Parameters	Values
V_{in}	240 V
f_s	10 kHz
$L_1 L_2$ *filter*	4 mH
C *filter*	3 μF
L converter side	5 mH
DC link	600V
Frequency	50 Hz
DC link Capacitance	5600 μF
System Capacity	6 kW
Battery Capacity	160 Ah
FOPID Gain (K_p, K_i, K_d)	1,10,0
FOPID Orders (μ, β)	0.5, 0.1

i Scenario 1, Grid-to-Vehicle (G2V)

Illustrates the measured voltage and current waveform over time, shown in Fig. 9. The voltage and current same phase, power supply to the grid-to-vehicle. The voltage exhibits a stable sinusoidal profile, while the current shows a lower amplitude with initial transient behaviour. The zoomed inset highlights steady-state phase characteristics, confirming periodic operation under balanced conditions.

Battery current and voltage responses over the time period 2 sec shown in Fig. 10. Both current and voltage are small disturbances at the starting point, from 0 to 0.05 sec. The battery current exhibits a brief transient before stabilizing near zero, while the battery voltage settles to a constant level after minor initial fluctuations, indicating stable conditions and effective system regulation.

Depicts the DC-link voltage response versus time, shown in Fig. 11. An initial overshoot and transient oscillation are observed at the starting point at 0 to 0.05 sec, followed by rapid convergence to a steady-

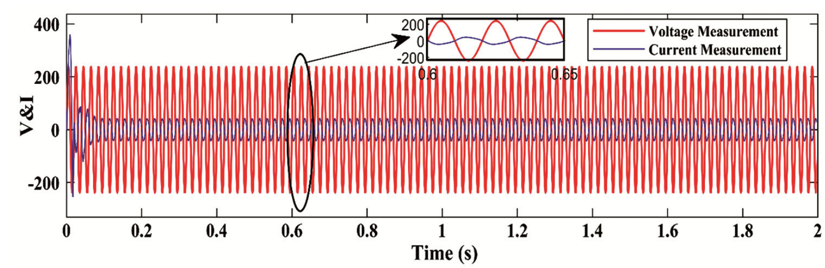

Fig. 9 — Performances of grid voltage and grid current under scenario-1

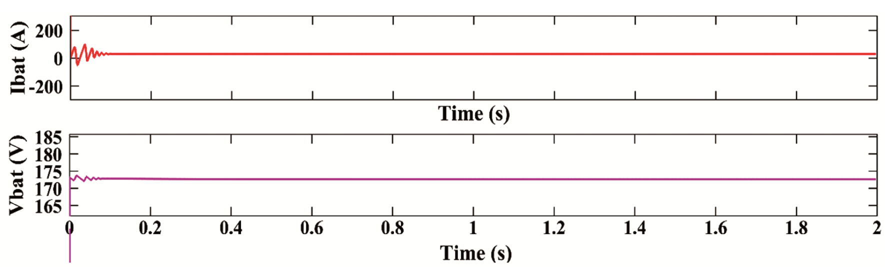

Fig. 10 — Performance of battery voltage and current under scenario-1

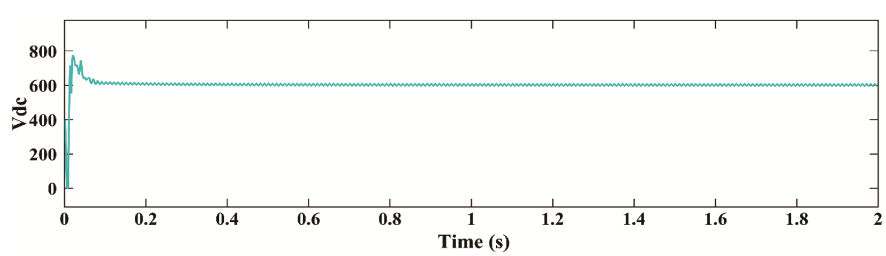

Fig. 11 — Performance of DC-link voltage under scenario-1

state value around the rated level. The minimal fast indicates effective voltage regulation and stable DC performance.

The change in the battery state of charge with time shown in Fig. 12. There is a progressive and almost linear reduction in SoC, suggesting regulated discharge of energy. The fact that there are no sharp shifts ensures that there were no operating conditions and successful control of power during the period of assessment.

ii Scenario 2, Vehicle-to-Grid (V2G)

The measured voltage and current waveform as a function of time shown in Fig. 13. The voltage and current are in the same phase, the power supply to the vehicle-to-grid, and the power factor is unity. An initial transient is observed, followed by steady-state sinusoidal operation. The voltage maintains a higher amplitude, while the current remains shifted with reduced magnitude, as highlighted in the magnified insert.

Battery current and voltage responses over the time period 2 sec in the V2G operating condition shown in Fig. 14. The battery current is -30 Amps, and the battery voltage is maintaining 173 volts. Both current and voltage are small disturbances at the starting point, from 0 to 0.05 sec. The battery current exhibits a brief transient before stabilizing near zero, while the battery voltage settles to a constant level after minor initial fluctuations, indicating stable conditions and effective system regulation.

Depicts the DC-link voltage response versus time, shown in Fig. 15. An initial overshoot and transient

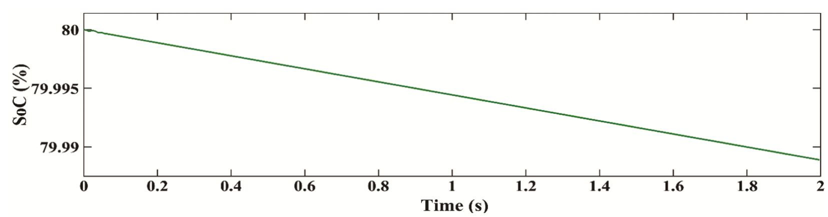

Fig. 12 — Performance of state of charge under scenario-1

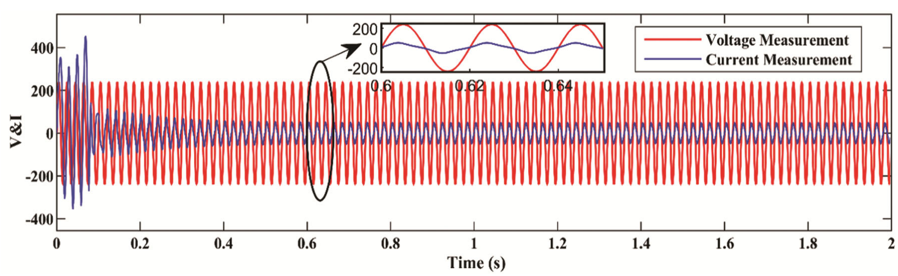

Fig. 13 — Performances of grid voltage and grid current under scenario-2

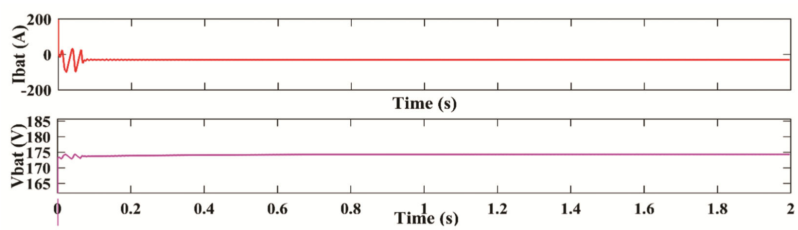

Fig. 14 — Performance of battery voltage and current under scenario-2

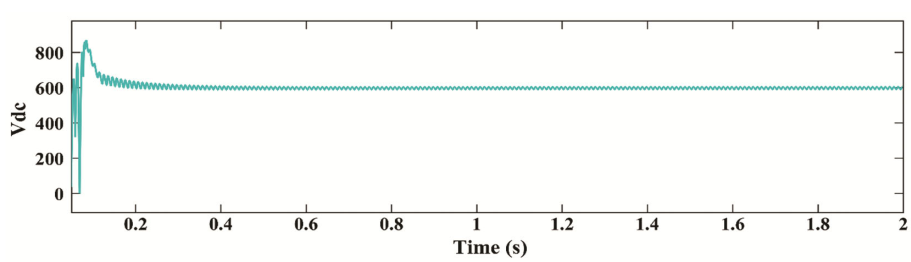

Fig. 15 — Performance of DC-link voltage under scenario-2

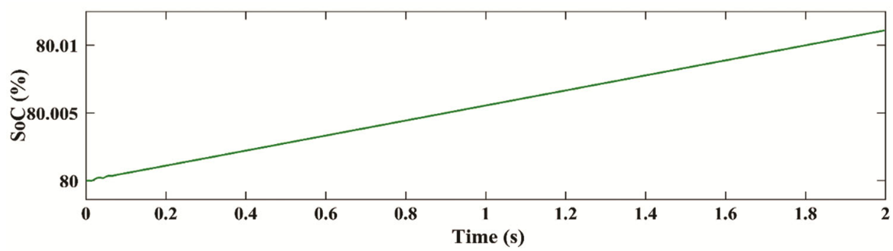

Fig. 16 — Performance of state of charge under scenario-2

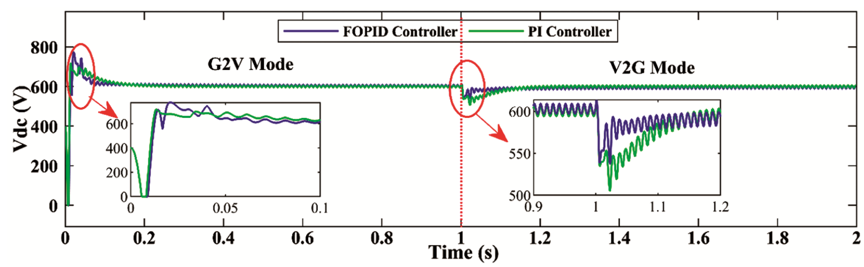

Fig. 17 — Comparison of DC-link voltage in proposed FOPID & PI controllers in scenario-3

oscillation are observed at the starting point at 0 to 0.05 sec, followed by rapid convergence to a steady-state value around the rated level. The minimal fast indicates effective voltage regulation and stable DC performance.

The change in the battery state of charge with time, Fig. 16. There is a progressive and almost linear increase in SoC, suggesting regulated discharge of energy. The fact that there are no sharp shifts ensures that there were no operating conditions and successful control of power during the period of assessment.

iii Scenario 3, Comparison of proposed FOPID and PI controller

Represent the DC-link (Vdc) response of the system in G2V and V2G mode of operation at the PI and FOPID controller shown in Fig. 17. The PI controller response in G2V operation demonstrates significant overshoot and longer stabilizing time, in comparison to the FOPID controller, which responds faster to voltage variation. There is a similar effect during V2G operation, with the PI controller oscillating more about the reference voltage. On the contrary, a FOPID controller offers a more linear control and better damping qualities. Compared analysis reveals that the FOPID controller improves the temporary performance and retains the voltage stability in the bidirectional power flow. These findings underscore the appropriateness of the FOPID method to the DC-link voltage regulation in electric vehicle charging systems that have to operate effectively and consistently in different modes.

The OPAL-RT is capable of validating the DC-link voltage at mode switching, as shown in Fig. 18. The

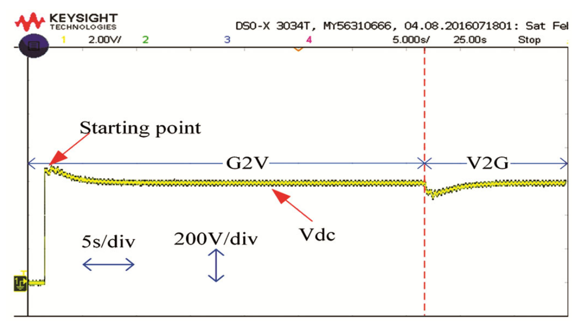

Fig. 18 — FOPID controller-based DC-link voltage validation in OPAL-RT

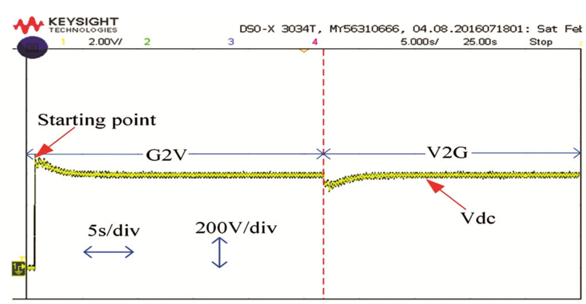

Fig. 19 — PI controller-based DC-link voltage validation in OPAL-RT

voltage quickly reaches a steady point after a transient at the point of operation. At the point of starting, a very small overshoot compared to the PI controller. The G2V operating stage is constant and has a small ripple. There is a slight notch when moving through the considerable switch to V2G, at which point the system begins the recovery process of meaning-controlled and consistent reaction.

The OPAL-RT is capable of validating the DC-link voltage at mode switching, as shown in Fig. 19. In

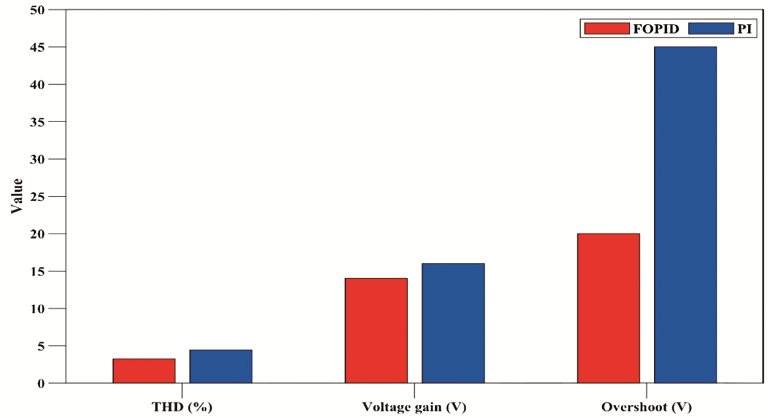

Fig. 20 — Comparative analysis of THD, Voltage gain and Overshoot in FOPID and PI

comparison to the FOPID controller-based DC-link voltage starting point, voltage overshoot and settling time are greater in G2V operating conditions. V2G operating condition, the undershoot and settling time are greater. A comparable FOPID controller-based system is more accurate and efficient.

The comparative analysis of THD, voltage gain and overshoot in FOPID and PI is shown in Fig. 20. The graph clearly shows that the THD of the PI controller and FOPID controller is 4.45 % and 3.24 %; the difference between the two controllers is 1.21 %. The voltage gain is PI and FOPID controllers is 16 V and 14 V, respectively. The difference between 2 V and the overshoot of both controllers is 20 V and 45 V, and the difference between 25 V. According to the analysis, the FOPID controller has better performance than the PI controller.

The comparative analysis of response time and settling time is shown in Fig. 21. The FOPID has a better response time of 0.01 sec, and the PI controller response time is 0.02 sec. The settling time of both controllers is 0.04 sec and 0.08 sec, respectively. The PI controller is more setting time of about 0.04 sec compared to the FOPID controller. In the proposed system, FOPID has better performance compared to the PI controller.

The efficiency graph of different controllers is shown in Fig. 22. The system efficiency is implemented in the PI controller and the proposed FOPID controller. It can be observed that the proposed controller enhances the efficiency in the case of FOPID in the load condition. In a PI controller, the system efficiency is 97.1 %, and in the proposed FOPID controller, it is 98.2 %. The difference between the two controllers' efficiency is about 1.1 %. It reduces energy consumption and enhances efficiency during charging and discharging conditions.

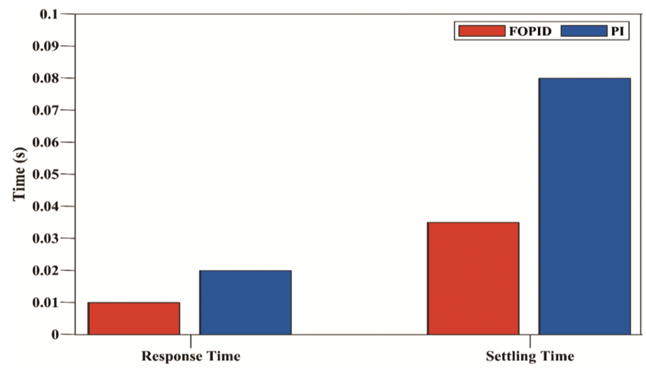

Fig. 21 — Comparative analysis of Response time and settling time

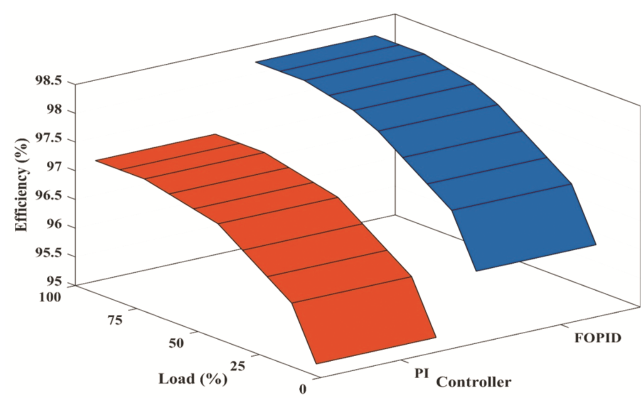

Fig. 22 — Efficiency graph between PI and proposed FOPID for outer-loop controller

The PI controller system has a THD of 4.45 %, indicating significant harmonic material and poor quality of the waveform. The use of the FOPID controller reduces THD to 3.24 %, as shown in Figs. 23 and 24. The THD reduction is 1.21 % to better performance. This is improved by the use of fractional-order dynamics that permit more flexible tuning and non-jumping system response. As a result,

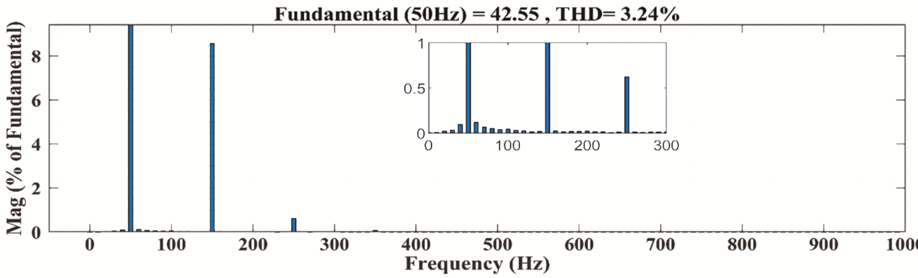

Fig. 23 — THD analysis of proposed FOPID controller G2V/V2G

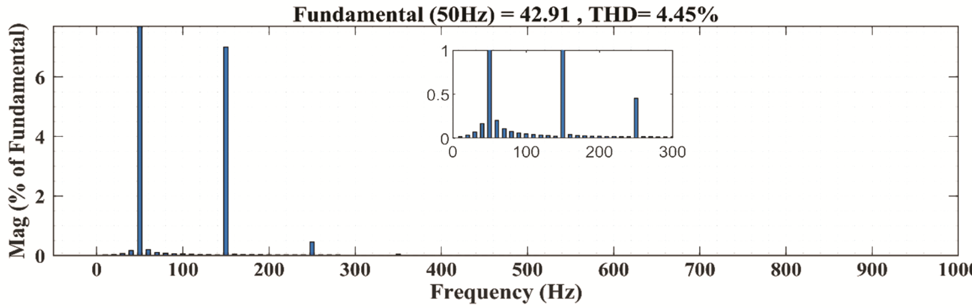

Fig. 24 — THD analysis of PI controller G2V/V2G

Table 2 — Comparison and performance analysis of proposed FOPID and PI controllers

Parameters	FOPID Controller	PI Controller
THD	3.24 %	4.45 %
Voltage gain	14 V	16 V
Overshoot	20 V	45 V
Response Time	0.01 sec	0.02 sec
Settling Time	0.04 sec	0.08 sec
Efficiency	98.2 %	97.1 %

Table 3 — List of acronyms

PEV	Plug-in Electric Vehicles	i_g	Grid current
G2V	Grid-to-Vehicle	V_c	Rms value
V2G	Vehicle-to-Grid	ω_g	Angular frequency
PI	Proportional–integral	θ	phase shift
v_{in}	Input voltage	$\pm h_i$	Tolerance Band
v_0	Output voltage	δ	phase angle
Vdc	DC-link voltage	V_{bat}	Battery voltage
ΔV_{dc}	Ripple of DC-link	I_{bat}	Battery current
V_{ref}	Reference Voltage	I_{cmd}	Battery charging current
FOPID	Fractional Order Proportional-Integral-derivative		

the FOPID controller enhances harmonic suppression, improves power quality, and ensures more stable and efficient system performance.

The comparative analysis of the proposed FOPID and conventional PI controllers is presented in Table 2. In a comparison of PI and FOPID controller-based systems, the PI controller-based system was observed to perform less than the FOPID. Compared to the PI controller, the THD of the FOPID controller is 1.21 % reduced. The voltage gain of the system is reduced by 2 V, the overshoot is 25 V, the response time is 0.01 sec, the settling time is 0.04 sec, and the efficiency is 1.1 %. Overall, the proposed FOPID is more accurate than the PI controller. The list of acronyms is presented in Table 3.

4 Conclusion

To enhance energy conversion efficiency, a DC-DC bidirectional converter is present in this work. The proposed FOPID controller is used as an outer-loop component to improve the system stability as well as the dynamic response. Therefore, the converter becomes appropriate for use in plug-in electric-vehicle applications that require improved battery performance. The applicability of the proposed methodology is supported by simulation studies and HIL validation. The measured values are the maximal voltage gain of up to 14 V, THD of 3.24 %, maximal overshoot of 25 V, response time of 0.01 s, settling time of 0.035 s and power-conversion efficiency of 98.2 %. These findings support that the system is able to significantly improve stability, as well as conversion efficiency. Future research will focus on more energy-management approaches and integration of inverters to fully utilize photovoltaic, wind, biomass, and energy-storage resources over a range of operating conditions.

References

1 Hafidh M Y, Wibawa U, Nurwati T & Wakama T E, *J Electr Electron Commun Control Inform Syst*, 17 (2023) 27.

2 Lee D, Kieu H P, Kim J, Choi S, Kim S & Martinez W, *IEEE Trans Ind Electron*, 71 (2024) 15815. Mamidala S & Kumar Y P, *Trans Energy Syst Eng Appl*, 5 (2024) 1.

3 Kancherla A B, Prasad N B & Kishore D R, *J Eng Appl Sci*, 71 (2024) 147.

4 Chaturvedi O K & Varsha Mehar M, *Res J Eng Tech Med Sci*, 7 (4) (2024).

5 Hemachandu P, Kusuma N, Sekhar A H, Sindhuja P D, Teja N R, Sharan M & Valavala M, In *2024 IEEE Int Conf Intell Syst Smart Green Technol*, (2024) p.56-59.

6 Prajapati B S & Singh R K, *J Power Electron*, 25 (4) (2025) 619.

7 Rana M M, Alam S M, Rafi F A, Deb S B, Agili B, He M & Ali M H, *IEEE Access*, 13 (2025) 35124.

8 Venkatesh C & Yesuraj S, *Electron Power Component Syst*, (2024) 1–21.

9 Santra S & De M, *Int J Robust Nonlinear Control*, 35 (17) (2025) 7215.

10 Islam M A, Singh J G, Jahan I, Lipu M H, Jamal T, Elavarasan R M & Mihet-Popa L, *IEEE Access*, 9 (2021) 166762.

11 Mohamed M, Alaas Z, Al Faiya B, Hegazy H Y, Mohamed W I & Abdelwahab S A M, *IEEE Access*, 13 (2025) 55996.

12 Warrier P & Shah P, *IEEE Access*, 9 (2021) 58982.

13 Nour M, Magdy G, Chaves-Ávila J P, Sánchez-Miralles Á & Petlenkov E, *IEEE Access*, 10 (2022) 51662.

14 Gül O & Garcia J L D, *IEEE Access*, 14 (2026) 4970.

15 Campos M W D S, Prado E M, De Medeiros R L, Fantesia M P, De Oliveira W D, Conceição V C & Ayres F A D C, *IEEE Trans Circuits Syst II: Express Briefs*, 72 (2025) 1218.

16 Gupta T N & Singh B, *IET Power Electron*, 14 (2) (2021) 313.

17 Verma A K, Singh B & Shahani D T, *International conference on energy, automation and signal*, (2011) 1-5.

18 Bialasiewicz J T, *IEEE Trans Ind Electron*, 55 (7) (2008) 2752.

19 Erickson R W & Maksimović D, *Fundamentals of Power Electronics* (Springer Science & Business Media, New York) 2007.

20 Kjaer S B, Pedersen J K & Blaabjerg F, *IEEE Trans Ind Appl*, 41 (5) (2005) 1292.

21 Panigrahi R, Mishra S K, Srivastava S C, Srivastava A K & Schulz N N, In *IEEE Trans Ind Appl*, 56 (3) (2020) 3178.

22 Jayalath S & Hanif M, *IEEE Trans Ind Electron*, 64 (3) (2017) 1905.

23 Mohanty S B, Mohanty S, Panda M & Dash S K, *Result Engineer*, 26 (2025) 105471.

24 Merai M, Naouar M W, Slama-Belkhodja I & Monmasson E, *IEEE Trans Ind Electron*, 66 (8) (2018) 6241.

25 Rani K S & Nandagopal V, *Electric Power Syst Res*, 252 (2026) 112262.

26 Saurabh K, Gupta N K & Singh A K, *7th International Conference on Signal Processing and Integrated Networks (SPIN)* (2020) 531.

27 Nippatla V R & Mandava S, *Results Engineer*, 26 (2025) 105460.

28 Li Z, Zang C, Zeng P, Yu H, Li S & Bian J, In *IEEE Trans Ind Electron*, 64 (5) (2017) 3862.